Weighted Time Warping Improves T-wave Morphology Markers Clinical Significance

Flavio Palmieri, Pedro Gomis, *IEEE Senior Member*, Dina Ferreira, Esther Pueyo, Juan Pablo Martínez, Pablo Laguna, *Fellow IEEE*, and Julia Ramírez

***Abstract*— *Background:* T-wave (TW) morphology indices based on time-warping (d_w) have shown significant cardiovascular risk stratification value. However, errors in the location of TW boundaries may impact their prognostic power. Our aim was to test the hypothesis that a weighted time-warping function (WF) would reduce the sensitivity of d_w to these errors and improve their clinical significance. *Methods:* The WFs were proportional to (i) the reference TW ($\mathcal{T}$), and (ii) the absolute value of its derivative ($\mathcal{D}$). The index d_w was recalculated using these WFs, and its performance was compared to the unweighted control case ($\mathcal{C}$) in four different scenarios: 1) robustness against simulated TW boundaries location errors; 2) ability to retain physiological information in an electrophysiological cardiac model; 3) ability to monitor blood potassium concentration changes ($\Delta[K^+]$) in 29 hemodialysis (HD) patients; 4) and the sudden cardiac death (SCD) risk stratification value of the TW morphology restitution (TMR) index, derived from d_w, in 651 chronic heart failure (CHF) patients. *Results and Discussion:* The WFs led to a reduced sensitivity ($\mathcal{R}$) of d_w to TW boundary location errors as compared to $\mathcal{C}$ (median $\mathcal{R}$=0.19 and 0.22 and 0.35 for $\mathcal{T}$, $\mathcal{D}$ and $\mathcal{C}$, respectively). They also preserved the physiological relationship between d_w and repolarization dispersion changes at ventricular level. No improvements in $\Delta[K^+]$ tracking were observed for the HD patients (Pearson's median correlation [r] between $\Delta[K^+]$ and d_w was $0.86 \leq r \leq 0.90$ for $\mathcal{T}$, $\mathcal{D}$ and $\mathcal{C}$). In CHF patients, the SCD risk stratification value of TMR was improved by applying $\mathcal{T}$ (hazard ratio, HAR, of 2.80), followed by $\mathcal{D}$ (HAR=2.32) and $\mathcal{C}$ (HAR=2.23). *Conclusions and Significance:* The proposed WFs, with $\mathcal{T}$ showing the best performance, increased the robustness of time-warping based markers against TW location errors preserving their physiological information content and boosting their SCD risk stratification value. Results from this work support the use of $\mathcal{T}$ when deriving d_w for future clinical applications.**

***Index Terms*— Electrocardiogram, T-wave time warping analysis, weighting functions, T-wave morphology, blood potassium concentration, sudden cardiac death**

F. Palmieri and P. Gomis are with Research Centre for Biomedical Engineering (CREB), Universitat Politècnica de Catalunya, Barcelona and with CIBER-BBN, Spain (e-mail: flavio.palmieri@upc.edu).
P. Gomis is with Universidad Internacional de Valencia, Valencia, Spain.
F. Palmieri and D. Ferreira are with Laboratorios Rubió S.A., Spain.
E. Pueyo, J. P. Martínez, and P. Laguna are with BSICoS group, I3A, IIS Aragón, University of Zaragoza, Zaragoza, and with CIBER-BBN, Spain.
J. Ramírez is with Aragon Institute of Engineering Research, University of Zaragoza, Zaragoza, Spain and William Harvey Research Institute, Queen Mary University of London, London, UK.

Copyright (c) 2021 IEEE. Personal use of this material is permitted. However, permission to use this material for any other purposes must be obtained from the IEEE by sending an email to pubs-permissions@ieee.org.

I. Introduction

THE electrocardiogram (ECG) is a non-invasive diagnostic tool that has substantial clinical impact on investigating and monitoring the severity of cardiovascular (CV) diseases [1]–[3]. Several T wave (TW)-derived indices, reflecting the repolarization of the ventricles [4], have been proposed for risk stratification, like the TW width [5], the distance from the peak to the end of the TW (T_{pe} interval) [6], the dynamics of the T_{pe} interval [7], the QT adaptation time [8], and the TW alternans [9]. However, these markers do not capture variations of the whole TW morphology, which has demonstrated improved capacity for risk stratification [10]–[12].

The TW morphology markers d_w^u [10] and d_w [13], quantifying the level of warping needed to temporally align two TWs, showed good correlation with dispersion of ventricular repolarization [10] and with blood potassium concentration ($[K^+]$) variations in hemodialysis (HD) patients [13]. Notably, the TW morphology restitution index (TMR), obtained from d_w^u, was found to be specifically associated with sudden cardiac death (SCD) in 651 chronic heart failure (CHF) patients (MUerte Súbita en Insuficiencia Cardiaca, MUSIC study) [11], and was significantly associated with CV risk in a middle-aged population undergoing an exercise stress test in the UK Biobank [12]. However, the computation of TW-based markers relies on the automatic location of TW onset and end timings, which might be challenging in the presence of ECG noise contamination, low TW amplitude or morphological variability [14], [15]. We hypothesized that adding a weighting stage to the calculation of d_w^u and d_w would attenuate the effects of potential location errors, maintaining their physiological relevance and, consequently, improving the SCD risk stratification value of the TMR.

The aim of this study was to propose two weighting functions (WFs) and thoroughly test their performance in four different scenarios: (1) an error-controlled simulated set up; (2) simulated ECGs from an electrophysiological cardiac model; (3) a dataset of 29 patients undergoing HD; and (4) in the MUSIC study.

II. Materials

A. Hemodyalisis dataset

The HD dataset population included 29 end-stage renal disease (ESRD) patients undergoing HD at the Nephrology ward at Hospital Clínico Universitario Lozano Blesa (Zaragoza,

Spain) as previously described in [13]. A 48-h, standard 12-lead ECG Holter recording (H12+, Mortara Instruments, Milwaukee, WI, USA, sampling frequency of 1 kHz, amplitude resolution of 3.75 μV) was collected from each patient, starting 5 min before the HD onset and lasting until the next HD session, scheduled 48 h later. Simultaneously, 5 blood samples were collected, from which 5 [K^+] was assessed before starting the HD (h_0) and at every hour during the HD session (h_1, h_2, h_3, h_4).

B. MUSIC dataset

A total of 992 patients with symptomatic CHF were enrolled in the MUSIC study, a prospective, multicenter study designed to assess risk predictors of CV mortality in ambulatory CHF patients [11]. Two-(3%) or 3-lead (97%) 24-h Holter ECG sampled at 200 Hz was recorded for each patient using ELA Medical equipment (Sorin Group, Paris, France). The study protocol was approved by the institutional investigation committees, and all patients signed informed consent [16]. Although the MUSIC study included patients in atrial fibrillation, sinus, flutter, and pacemaker rhythm, in the present study we only analyzed the ECG from the 651 patients in sinus rhythm.

Follow-up visits were conducted on an outpatient basis for a median of 44 months. Subjects were classified as SCD, cardiac death (CD), pump failure death (PFD) and survivors. CD was defined as SCD if it was (1) a witnessed death occurring within 60 minutes of the onset of new symptoms, unless a cause other than cardiac was obvious; (2) an unwitnessed death (< 24 hours) in the absence of preexisting progressive circulatory failure or other causes of death; or (3) a death during attempted resuscitation. Deaths occurring in hospitals as a result of refractory progressive end-stage CHF were defined as PFD [16].

As previously done in [11], we considered in the group of non cardiac event (non-CE) the aggregation of survivors and non-CD, and as non-SCD the aggregation of non-CE and PFD. The number of patients in each group (SCD, PFD and non-CE) and the number of patients with two or three recorded leads are given in Table I.

TABLE I: Characteristics of the analyzed MUSIC dataset: number of patients in sinus rhythm for each considered group (i.e. SCD, PFD and non-CE) and number of records with two or three leads.

Classification Criteria	Clinical outcome			#ECG leads	
Group	SCD	PFD	non-CE	3 leads	2 leads
# Patients	55	67	529	630	21

III. Methods

A. ECG Pre-processing

Preprocessing of the ECG signals included low-pass filtering at 40 Hz with a 6-th order Butterworth filter to remove electric and muscle noise, allowing QRS detection, cubic splines interpolation for baseline wander removal, and ectopic beats detection [10]. A single-lead QRS detection and TW delineation was performed, followed by a multi-lead strategy for global TW delineation [17]. Then, Principal Component Analysis (PCA) was applied lead-wise, learned over the segmented TWs, to generate a transformed lead with emphasised TW components. The TWs of the first PCA (PC1) were further delineated and smoothed by applying a 12-th order Butterworth 20 Hz low-pass filter to remove remaining noise components outside the TW frequency band.

B. Time-warping markers definition

Let $\boldsymbol{f}^r(\boldsymbol{t}^r)$ be the reference TW and $\boldsymbol{f}^s(\boldsymbol{t}^s)$ the TW under study (Fig. 1a, blue and red TW respectively), with $\boldsymbol{t}^r = \begin{bmatrix} t^r(1) & \cdots & t^r(N_r) \end{bmatrix}^\top$ and $\boldsymbol{t}^s = \begin{bmatrix} t^s(1) & \cdots & t^s(N_s) \end{bmatrix}^\top$ their time samples, of length N_r and N_s, respectively.

Let $\gamma(\boldsymbol{t}^r)$ be the warping function that relates $\boldsymbol{t}^r$ and $\boldsymbol{t}^s$ such that the composition $[\boldsymbol{f}^s \circ \gamma](\boldsymbol{t}^r) = \boldsymbol{f}^s(\gamma(\boldsymbol{t}^r))$ denotes the re-parameterization, or time domain warping, of $\boldsymbol{f}^s(\boldsymbol{t}^s)$ using $\gamma(\boldsymbol{t}^r)$. The warping information (green area in Fig. 1d) was quantified as:

$$d_w^u = \frac{1}{N_r} \sum_{n=1}^{N_r} |\gamma^*(t^r(n)) - t^r(n)|, \tag{1}$$

where $\gamma^*(\boldsymbol{t}^r)$ is the optimal warping function relating $\boldsymbol{f}^r(\boldsymbol{t}^r)$ to $\boldsymbol{f}^s(\boldsymbol{t}^s)$ (Fig. 1d dashed red line) [10]. Similarly, the signed version, d_w, was quantified as in [13]:

$$d_w = \left(\frac{s_d}{|s_d|} \right) \frac{1}{N_r} \sum_{n=1}^{N_r} |\gamma^* \left(t^r \left(n\right)\right) - t^r \left(n\right)| \tag{2}$$

$$s_d = \sum_{n \in N_r^u} \left(\gamma^* \left(t^r \left(n\right)\right) - t^r \left(n\right)\right) + \sum_{n \notin N_r^u} \left(t^r \left(n\right) - \gamma^* \left(t^r \left(n\right)\right)\right) \tag{3}$$

being N_r^u the set of up-slope samples [13]. The sign, s_d, was computed in the control case ($\mathcal{C}$) with no weighting, $\mathcal{W}_\mathcal{C}(\boldsymbol{t}^r) = \mathbf{1}$, and then applied to d_w obtained with and without weighting.

C. Weighting functions

Aiming to attenuate the undesired effects caused by TW delineation errors on the computation of d_w^u and d_w, two different WFs were used to emphasize the TW peak and the regions of maximum slope, respectively, while attenuating both ends.

The first WF, $\mathcal{W}_\mathcal{T}(\boldsymbol{t}^r)$, was taken as the normalized reference TW itself, obtained by dividing $\boldsymbol{f}^r(\boldsymbol{t}^r)$ by its maximum value (Fig. 1b, blue TW). Then, the linear function connecting the first and last samples was subtracted (Fig. 1b, magenta), obtaining the green TW (Fig. 1b), which later was also normalized by its maximum value, resulting in the final $\mathcal{W}_\mathcal{T}(\boldsymbol{t}^r)$ (Fig. 1b, black).

The second WF, $\mathcal{W}_\mathcal{D}(\boldsymbol{t}^r)$, was taken as the derivative of the reference TW and computed as follows. First, the absolute value of the derivative of the reference TW, $\boldsymbol{f}^r(\boldsymbol{t}^r)$, was divided into two halves, with the middle zero value (corresponding to the $\boldsymbol{f}^r(\boldsymbol{t}^r)$ peak) taken as the splitting point. Then, the same procedure previously described for $\mathcal{W}_\mathcal{T}(\boldsymbol{t}^r)$

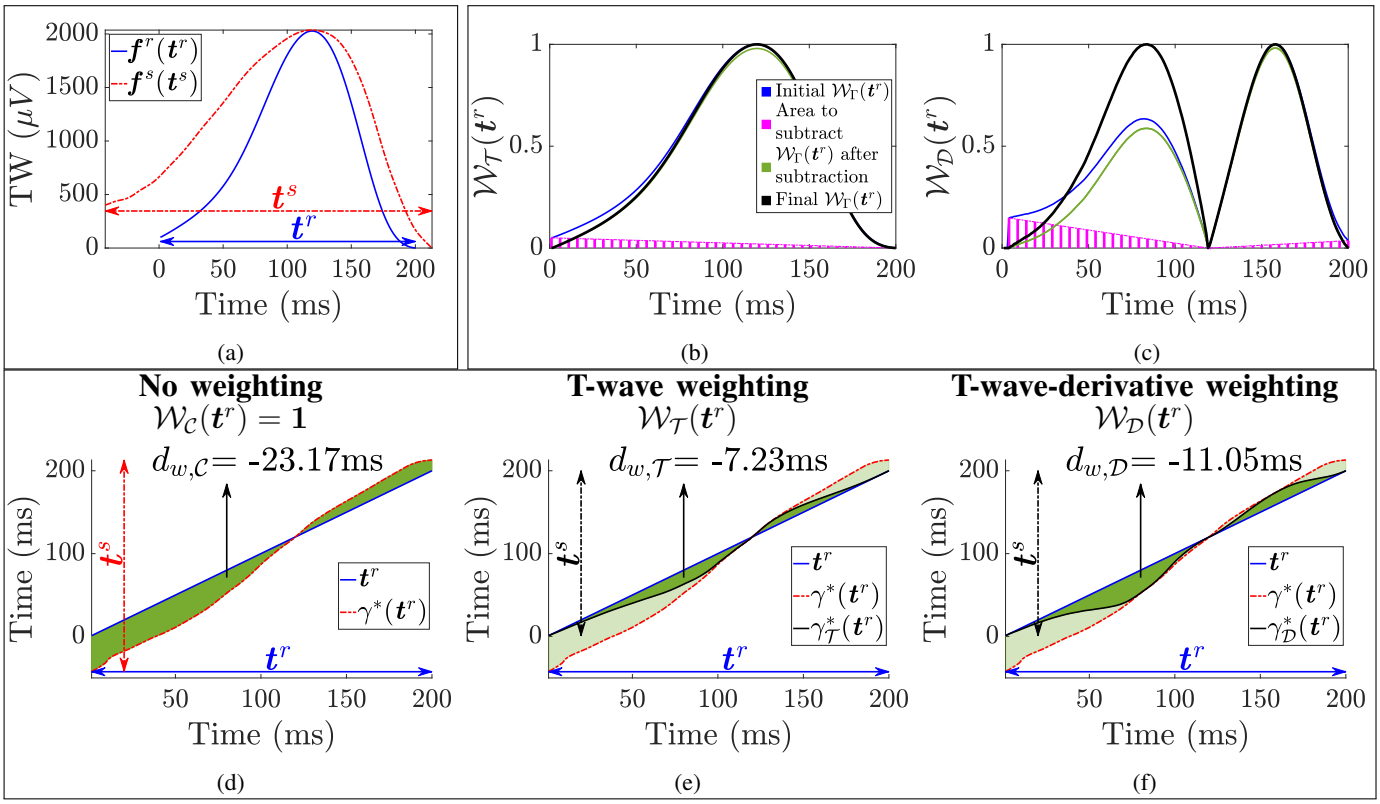

Fig. 1: Illustration of the proposed weighting functions $\mathcal{W}_\Gamma(t^r)$, $\Gamma \in \{\mathcal{C}, \mathcal{T}, \mathcal{D}\}$, and application for d_w computation. Panel (a) shows the reference and studied TW (blue and red, respectively). Panels (b) and (c) show the process to derive $\mathcal{W}_\mathcal{T}(t^r)$ and $\mathcal{W}_\mathcal{D}(t^r)$, respectively, as detailed in section III-C. Panel (d) shows the calculation of the control $d_{w,\mathcal{C}}$ (dark green area under $\gamma^*(t^r)$), while panels (e) and (f) show the calculation of $d_{w,\mathcal{T}}$ and $d_{w,\mathcal{D}}$, estimated by using $\gamma^*_\mathcal{T}(t^r)$ and $\gamma^*_\mathcal{D}(t^r)$, respectively computed as in eq. (4), obtaining the updated dark green areas.

was individually applied to each half. Finally, the two parts were linked, obtaining $\mathcal{W}_\mathcal{D}(t^r)$ (Fig. 1c).

The $\gamma^*(t^r)$ function was then multiplied by each WF

$$\gamma^*_\Gamma(t^r) = \gamma^*(t^r) \cdot \mathcal{W}_\Gamma(t^r), \tag{4}$$

being $\Gamma \in \{\mathcal{C}, \mathcal{T}, \mathcal{D}\}$. The resulting $\gamma^*_\mathcal{T}(t^r)$ and $\gamma^*_\mathcal{D}(t^r)$ are depicted in Fig. 1e and Fig. 1f (black solid line) respectively. Finally, both d^u_w and d_w were re-computed. We denoted markers d^u_w and d_w extracted in the control case as $d^u_{w,\mathcal{C}}$ and $d_{w,\mathcal{C}}$, respectively, while as $d^u_{w,\mathcal{T}}$ ($d_{w,\mathcal{T}}$) and $d^u_{w,\mathcal{D}}$ ($d_{w,\mathcal{D}}$) those after weighting with $\mathcal{W}_\mathcal{T}(t^r)$ and $\mathcal{W}_\mathcal{D}(t^r)$, respectively. The resulting $d_{w,\mathcal{T}}$ and $d_{w,\mathcal{D}}$, quantifying the weighted dark green area, are depicted in Fig. 1e and Fig. 1f, respectively.

D. Simulation of TW boundaries shift

To assess the impact of TW boundaries shift on the calculation of d^u_w and d_w with and without applying the proposed WFs, a study simulating controlled variations in the TW duration and amplitude at different levels of TW boundaries shift was performed.

1) TW modulation: A reference TW, $\boldsymbol{f}^r(t^r)$, was extracted from PC1 of a clean 12-lead ECG sampled at 1 kHz from a healthy subject [18]. Then, a set of K = 300 TWs modulated in amplitude and duration were generated, as in [10], according to the following steps:

i. Adding amplitude variability. Nonlinear TW amplitude variability was introduced as:

$$\boldsymbol{f}^s_{\mathrm{NL},k}(t^r) = \boldsymbol{f}^r(t^r) + c(k)\sin\left(2\pi\frac{1}{4N_r}t^r\right),$$
$$c(k) = 150\sin\left(\frac{\pi\left(\frac{K}{2}+k-1\right)}{K}\right), \quad k = 1, \cdots, K \tag{5}$$

with N_r and t^r defined in section III-B and k the TW index. Next, TW linear amplitude variability was modeled multiplying the deviations from the isoelectric line of $\boldsymbol{f}^s_{\mathrm{NL},k}$ by a factor sinusoidally modulated across TW:

$$\boldsymbol{f}^s_{\mathrm{L},k}(t^r) = \left(1 + 0.15\sin\left(\frac{\pi\left(\frac{K}{2}+k-1\right)}{K}\right)\right)\boldsymbol{f}^s_{\mathrm{NL}}(t^r) \tag{6}$$

ii. Adding time variability. Linear variations in the time of the TW were simulated as in following equations:

$$\boldsymbol{t}^s_{\mathrm{L},k} = \gamma_k(t^r), \quad k = 1, \cdots, K \tag{7}$$

where $\gamma_k(t^r)$ resamples t^r based on the factor $\alpha(k)$ [10]:

$$\alpha(k) = \frac{0.6 \cdot (k-1)}{K-1} + 0.7, \quad k = 1, \cdots, K \tag{8}$$

Nonlinear variations in the temporal domain of the TW were introduced by adding a sinusoidal modulation of

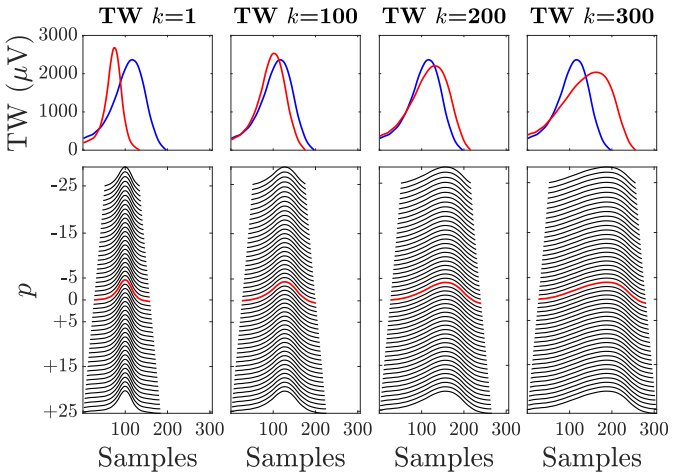

Fig. 2: Simulated TW variations (upper panels) and their corresponding boundaries shift with symmetrically modified T_o and T_e boundaries (lower panels). The reference $\boldsymbol{f}^r(\boldsymbol{t}^r)$ is displayed in blue and the modulated $\boldsymbol{f}^s_k(\boldsymbol{t}^s)$ (see eq. (10)) is plotted in red for $k = 1, 100, 200$ and 300 in upper panels. Lower panels show the resulting TWs after shifting T_o and T_e symmetrically by removing (adding) up to p=25 samples, being in red the modulated $\boldsymbol{f}^s_k(\boldsymbol{t}^s)$ without shift (i.e. p=0).

period N_r and linearly varying amplitude, guaranteeing a monotonic increasing function:

$$\begin{aligned} \boldsymbol{t}^s_k &= \boldsymbol{t}^s_{\mathrm{L},k} + \beta(k)\frac{N_r}{N_s}\cdot\sin\left(2\pi\frac{1}{N_r}\boldsymbol{t}^s_{\mathrm{L},k}\right), \\ \beta(k) &= \frac{30(k-1)}{K-1} - 15, \quad k = 1,\cdots,K \end{aligned} \tag{9}$$

The whole TW duration and amplitude variability can be expressed as:

$$\boldsymbol{f}^s_k(\boldsymbol{t}^s) = \boldsymbol{f}^s_{\mathrm{L},k}\left(\gamma_k(\boldsymbol{t}^r) + \beta(k)\frac{N_r}{N_s}\cdot\sin\left(2\pi\frac{1}{N_r}\gamma_k(\boldsymbol{t}^r)\right)\right) \tag{10}$$

The upper panels in Fig. 2 show the resulting modulated TWs for $k = 1, 100, 200$ and 300.

2) Boundaries shift: For each of the K=300 modulated $\boldsymbol{f}^s_k(\boldsymbol{t}^s)$, we simulated TW boundary location errors to: (1) T onset (T_o) only, (2) T end (T_e) only and (3) both T_o and T_e positions symmetrically. In each test, p samples, ranging from p=1 up to p=25, were progressively removed (added). Therefore, for each $\boldsymbol{f}^s_k(\boldsymbol{t}^s)$, a total of 50 boundary-shifted TWs were generated, having a boundary location standard deviation of $\sigma = 14.9$ ms, a value within the manual TW end determination tolerance [19]. Lower panels in Fig. 2 show the symmetrical T_o and T_e shift when $k = 1, 100, 200$ and 300.

Then, markers $d^u_{w,\Gamma}$ and $d_{w,\Gamma}$ were evaluated by time warping each boundary-shifted $\boldsymbol{f}^s_k(\boldsymbol{t}^s)$ and the reference $\boldsymbol{f}^r(\boldsymbol{t}^r)$. Finally, for every test (i.e. shift of T_o only, T_e only and T_o-T_e symmetrically), a variation ratio ($\mathcal{R}$) was computed for each $\boldsymbol{f}^s_k(\boldsymbol{t}^s)$ and WF as:

$$\mathcal{R}_{\Gamma,k} = \frac{\sigma(d_{\Gamma,k}(p))}{|d_{\Gamma,k}(p=0)|}, \tag{11}$$

where $k = 1,\cdots,300$ accounts for the modulated TW, $p \in \{-25,\cdots,25\}$ denotes the samples added (removed), $d \in \{d^u_w, d_w\}$, $\Gamma \in \{\mathcal{C},\mathcal{T},\mathcal{D}\}$, $d_{\Gamma,k}(p{=}0)$ is the marker value computed when no shift is performed and $\sigma(d_{\Gamma,k}(p))$ is the standard deviation of the marker series for kth simulated TW.

E. Simulated variability in an electrophysiological model

To assess whether using the proposed WFs affects the relationship between changes in myocardial repolarization dynamics and d^u_w [10] and d_w, an electrophysiological model [20] was used.

This equivalent double layer model formalizes the forward problem in which action potentials at M ventricular sites are projected onto the body surface. The action potentials repolarization time at each cardiac site m is given by $\rho_m = \bar{\rho} + \Delta\rho_m$, where $\bar{\rho}$ is the spatial mean repolarization time and $\Delta\rho_m$ represents the deviation from $\bar{\rho}$ at site m. The standard deviation of $\Delta\rho_m$, σ, is a measure of the global dispersion of repolarization. Ventricular action potential data was obtained from a normal male, and the ECG leads were calculated as described in [10]. Spatial PCA was performed on the resulting ECG leads, and the PC1 was preprocessed and delineated (see section III-A). The extracted TW was taken as the reference in this simulation study.

A total of five different TWs, $j = 1,\cdots,5$, were, then, generated by varying the level of σ in two scenarios:

i. Varying the repolarization time dispersion, σ:

$$\sigma(j) = \sqrt{\frac{1}{M-1}\sum_{m-1}^{M}(\Delta\rho_m(j))^2}, \quad j = 1,\cdots,5, \tag{12}$$

with $\Delta\rho_m(j) = \Delta\rho_m(1 + 0.2(j-1))$, expressed in ms.

ii. Varying σ as in eq. (12), simultaneously with the lengthening of the mean repolarization time $\bar{\rho}$, according to:

$$\bar{\rho}(j) = \bar{\rho} + 25\cdot(j-1), \quad j = 1,\cdots,5. \tag{13}$$

The resulting $d^u_{w,\Gamma}(j)$ and $d_{w,\Gamma}(j)$ were computed by warping each jth TW with the reference TW, which for both scenarios corresponds to the TW when j=1, and plotted with respect to σ to infer the influence of the proposed WFs.

F. Hemodyalisis Dataset

To evaluate the influence of the proposed WFs on the reported ability of d_w and d^u_w to track [K^+] variations [13], correlation between serum [K^+] and $d^u_{w,\Gamma}$ and $d_{w,\Gamma}$ was reestimated.

As in [13], TWs in 2-min windows centered around the 5-th and 35-th minutes of each available hour were selected and a mean warped TW (MWTW) was computed from the TWs in each window [10], [13]. Then, $d^u_{w,\Gamma}$ and $d_{w,\Gamma}$ were computed by time warping each MWTW with respect to a reference MWTW, selected at the HD end (h_4).

The correlation between the relative variation of [K^+], $\Delta[K^+]$, and $d^u_{w,\Gamma}$ and $d_{w,\Gamma}$ was evaluated by Pearson correlation (r) and compared for each of the different WF strategies. $\Delta[K^+]$ was defined as:

$$\Delta[K^+](h_i) = [K^+]_{h_i} - [K^+]_{h_4}, \tag{14}$$

being $[K^+]_{h_i}$ the concentration at the h_ith time point (h_0 to h_4), and $[K^+]_{h_4}$ the reference [K$^+$] at the end of the HD (h_4).

G. MUSIC dataset

To determine if the proposed WFs can improve the SCD risk stratification value of TMR [11], we recalculated TMR using $d^u_{w,\Gamma}$ and $d_{w,\Gamma}$ following these main steps [11]:

i. RR histogram construction. The histogram of the RR intervals for all beats in the 24-h Holter ECG was obtained, considering bins with a width of 10 ms (Fig. 3a). RR bins with fewer than 50 occurrences (dot orange line in Fig. 3a) were not considered in the following analysis.

ii. Intrasubject RR range definition. The median RR was identified (Fig. 3a, green bin). Then, the two most distant RR bins from the median, distributed symmetrically around it, were chosen as those defining the maximum intrasubject RR range, ΔRR. Then, naming RR$_{\text{max}}$ (Fig. 3a, red bin) and RR$_{\text{min}}$ (Fig. 3a, blue bin) respectively the maximum and the minimum RR:

$$\Delta\text{RR} = \text{RR}_{\text{max}} - \text{RR}_{\text{min}} \tag{15}$$

iii. The MWTWs of the TWs in the RR$_{\text{min}}$ and RR$_{\text{max}}$ bins were computed (Fig. 3b and Fig. 3c respectively) as the average TW morphology in those bins [10]. Then, time warping markers $d^u_{w,\Gamma}$ and $d_{w,\Gamma}$ were computed.

iv. TMR index was calculated dividing $d^u_{w,\Gamma}$, or $d_{w,\Gamma}$, by ΔRR, giving information on the TW morphological change per RR increment:

$$\text{TMR}^u_\Gamma = \frac{d^u_{w,\Gamma}}{\Delta\text{RR}}, \quad \text{TMR}_\Gamma = \frac{d_{w,\Gamma}}{\Delta\text{RR}} \tag{16}$$

The Mann-Whitney test was used to evaluate the association of both TMR$^u_\Gamma$ and TMR$_\Gamma$ with SCD and PFD. Receiver operating characteristic (ROC) curves were used to test the ability to predict SCD and to set cutoff points for risk stratification. The population was divided into 5 equally sized groups with similar SCD and non-SCD ratio, and in each group, the criterion of minimal Euclidean distance from each ROC curve to the upper-left corner was applied to select the optimal threshold within each group [11], [21]. This was repeated 10 times, and the mean and standard deviation (std) of the AUCs, the median and interquartile range (IQR) of the optimal thresholds and the accuracy were calculated.

Survival probability, performed by using the median optimal threshold, was estimated by Kaplan-Meier methods [22], [23], comparison of cumulative events was performed by using log-rank (Mantel-Cox) tests and risk evaluation was quantified by Cox proportion hazard test [24], [25]. Patients who died from causes other than SCD were censored at the time of death. A p-value (p-val)$<$0.05 was considered as statistically significant.

IV. Results

A. Simulation of TW boundaries shift

Distributions of $\mathcal{R}_{\Gamma,k}$ obtained when $d = d^u_w$ and $d = d_w$ are depicted in Fig. 4a and Fig. 4b, respectively. In each panel, the three tests (i.e. shift of T_o only, T_e only and T_o-T_e symmetrically) are shown, being the green, purple and orange

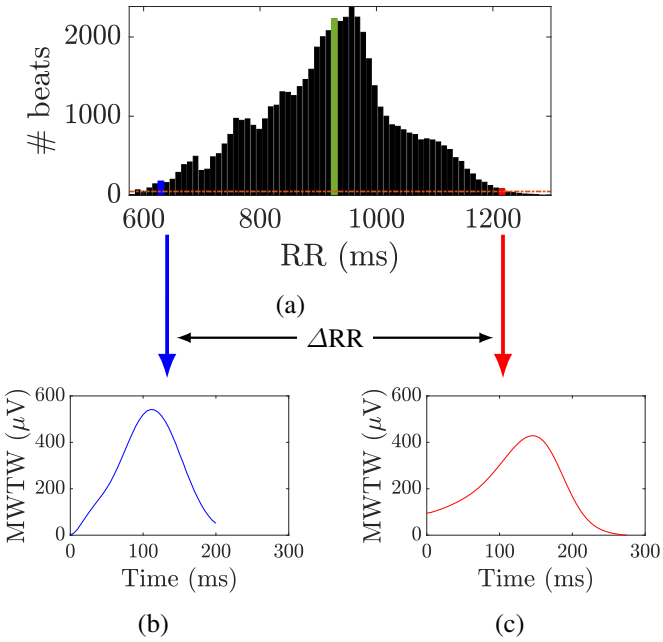

Fig. 3: Estimation of MWTWs in the MUSIC dataset. Panel (a) shows the RR histogram for a given patient with bins of 10 ms width. The green bin denotes the median RR interval, while the blue and red bins correspond to those RR intervals defining the maximum intrasubject range, ΔRR. The orange line denotes the #50-threshold limit. Panels (b) and (c) plot the MWTWs of the TWs included in the selected RR bins in (a).

boxplots the distributions resulting when $\mathcal{W}_\mathcal{C}(\boldsymbol{t}^r)$, $\mathcal{W}_\mathcal{T}(\boldsymbol{t}^r)$ and $\mathcal{W}_\mathcal{D}(\boldsymbol{t}^r)$ are applied respectively.

B. Simulated variability in electrophysiological model

Simulated TWs and their corresponding $d^u_{w,\Gamma}$ and $d_{w,\Gamma}$ values were obtained as described in section III-E. For the first considered scenario (i.e. only varying σ) results are presented in Fig. 5 (a)-(c); while those for the second scenario (i.e. combined variations in σ and $\bar{\rho}$) are in Fig. 5 (d)-(f).

C. Hemodyalisis dataset

Distributions of $\Delta[K^+]$, $d^u_{w,\Gamma}$ and $d_{w,\Gamma}$ across patients for every hour h_i during HD therapy are depicted in Fig. 6a and Fig. 6b, respectively. In each panel, the blue boxplots represent $\Delta[K^+]$ and referred to the left y-axis, while the corresponding makers are referred to the right y-axis and depicted in green ($\Gamma = \mathcal{C}$), purple ($\Gamma = \mathcal{T}$) and orange ($\Gamma = \mathcal{D}$).

Median (IQR) values for Pearson correlation between $\Delta[K^+]$ and every $d^u_{w,\Gamma}$ and $d_{w,\Gamma}$ are presented in Table II.

D. MUSIC dataset

Distributions of TMR$^u_\Gamma$ and TMR$_\Gamma$ are presented in Fig. 7a and Fig. 7b, respectively. Boxplots are shown in purple for $\mathcal{W}_\mathcal{T}(\boldsymbol{t}^r)$, in orange for $\mathcal{W}_\mathcal{D}(\boldsymbol{t}^r)$ and in green for the $\mathcal{W}_\mathcal{C}(\boldsymbol{t}^r)$ case. Patients are grouped according to their outcomes (i.e. SCD, PFD and non-CE). Significant Mann-Whitney test p-val (see Fig. 7) was found for each TMR$^u_\Gamma$ and TMR$_\Gamma$ when

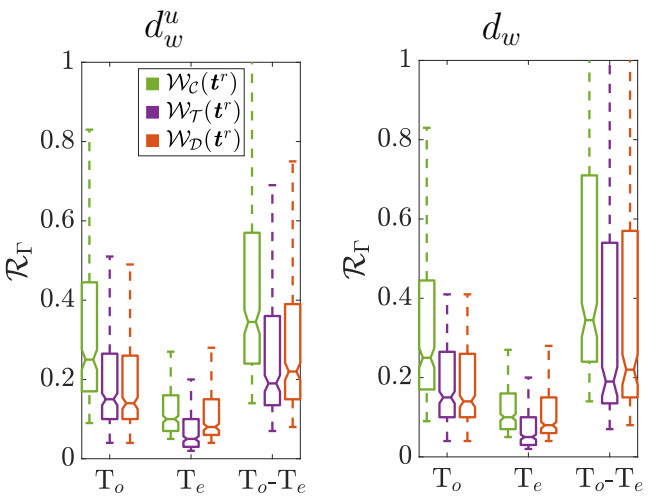

(a) (b)

Fig. 4: Distribution of $\mathcal{R}_{\Gamma,k}$ for each shift test (T_o only, T_e only and T_o-T_e symmetrically), marker and WF. In each panel, the green, purple and orange boxplots represent distributions for $\mathcal{W}_\mathcal{C}(\boldsymbol{t}^r)$, $\mathcal{W}_\mathcal{T}(\boldsymbol{t}^r)$ and $\mathcal{W}_\mathcal{D}(\boldsymbol{t}^r)$, respectively.

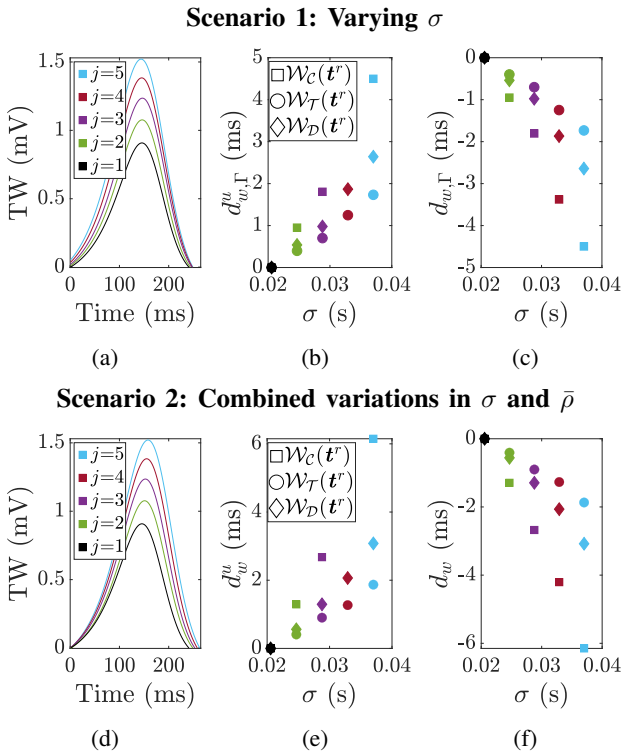

(a) (b) (c)

(d) (e) (f)

Fig. 5: Performance evaluation using the electrophysiological cardiac model (section III-E). Panels (a)-(c) show the results when only σ is varied in the model; while panels (d)-(f) show the combined variation of σ and $\bar{\rho}$. Panels (a) and (d) plot the TWs; while $d_{w,\Gamma}^u$ and $d_{w,\Gamma}$ values for both scenarios are shown in panels (b), (e), (c) and (f). Square, circle and diamond-shaped markers denote results for $\mathcal{W}_\mathcal{C}(\boldsymbol{t}^r)$, $\mathcal{W}_\mathcal{T}(\boldsymbol{t}^r)$ and $\mathcal{W}_\mathcal{D}(\boldsymbol{t}^r)$, respectively. Each colour denotes results for the jth TW, corresponding to a particular σ, computed as in eq. (12) and eq. (13) (scenarios 1 and 2, respectively).

comparing SCD victims and non-SCD patients regardless of the employed WF, while difference between PFD and non-CE were no significant. Finally, a statistical difference between SCD and PFD was only found for the TMR_Γ index.

Table III shows the mean and standard deviation (std) of the area under the curve (AUC) from the ROC curve analysis, median (IQR) for the optimal thresholds for SCD risk stratification and the accuracy evaluated for TMR_Γ^u and TMR_Γ indexes.

Fig. 8 plots the Kaplan-Meier survival probability curves obtained after dichotomizing the study population based on the optimal thresholds for TMR_Γ^u and TMR_Γ.

TABLE II: Pearson correlation (r) median (IQR) values across patients computed between $\Delta[K^+]$ and each $d_{w,\Gamma}^u$ and $d_{w,\Gamma}$.

	Γ	r
$d_{w,\Gamma}^u$	$\mathcal{C}$	0.92 (0.36)
	$\mathcal{T}$	0.88 (0.36)
	$\mathcal{D}$	0.92 (0.40)
$d_{w,\Gamma}$	$\mathcal{C}$	0.89 (0.35)
	$\mathcal{T}$	0.86 (0.36)
	$\mathcal{D}$	0.90 (0.39)

TABLE III: AUC, mean (std), and optimal thresholds (THR), median (IQR), for each TMR_Γ^u and TMR_Γ. The accuracy is included for a THR derived from the complete date set.

	Γ	AUC mean (std)	Optimal THR median (IQR)	Accuracy
TMR_Γ^u	$\mathcal{C}$	0.62 (0.10)	0.045 (0.012)	0.59
	$\mathcal{T}$	0.58 (0.10)	0.012 (0.005)	0.65
	$\mathcal{D}$	0.60 (0.10)	0.021 (0.004)	0.68
TMR_Γ	$\mathcal{C}$	0.64 (0.08)	-0.045 (0.010)	0.63
	$\mathcal{T}$	0.62 (0.10)	-0.012 (0.002)	0.69
	$\mathcal{D}$	0.63 (0.09)	-0.021 (0.004)	0.70

V. Discussion

In this study, we proposed and introduced, for the first time, two WFs to attenuate the effects of TW location errors. Using these WFs, we recalculated two TW morphology indices, $d_{w,\Gamma}$ and $d_{w,\Gamma}^u$, and we thoroughly evaluated: their robustness against simulated TW boundaries location errors, their physiological relevance in an electrophysiological model and in an HD dataset, and their SCD risk stratification value. Our main findings were that the WFs reduce the effects of TW boundaries location errors, with no impact in the ability of d_w^u and d_w to reflect repolarization dispersion, but significantly boosting their SCD risk stratification value. However, no meaningful changes in monitoring $[\text{K}^+]$ were found.

A. Simulation of TW boundaries shift

The purpose of this analysis was to evaluate the ability of the WFs in reducing the undesired effects of TW boundaries misplacement under controlled conditions in three possible scenarios: misplacement of just one extreme, either T_o or T_e, and both of them symmetrically.

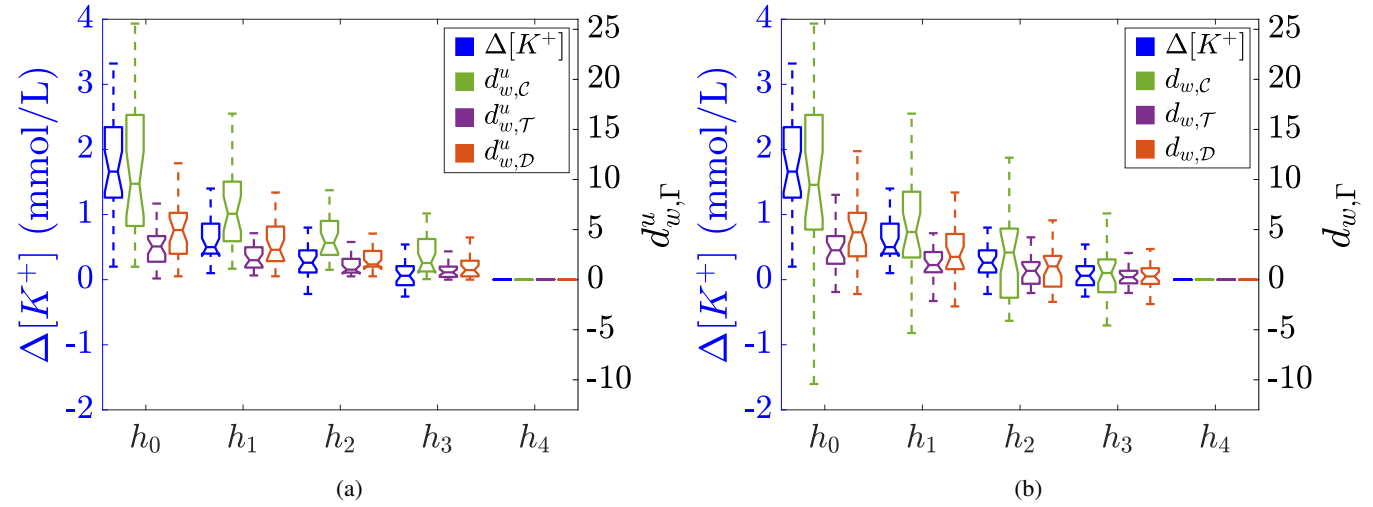

Fig. 6: Distribution of $\Delta[K^+]$ (blue, left y-axis), and $d^u_{w,\Gamma}$ (panel (a)) and $d_{w,\Gamma}$ (panel (b)) for each WF ($\Gamma \in \{\mathcal{C}, \mathcal{T}, \mathcal{D}\}$ green, purple and orange boxplot, respectively, right y-axis), during the HD session from h_0 to h_4.

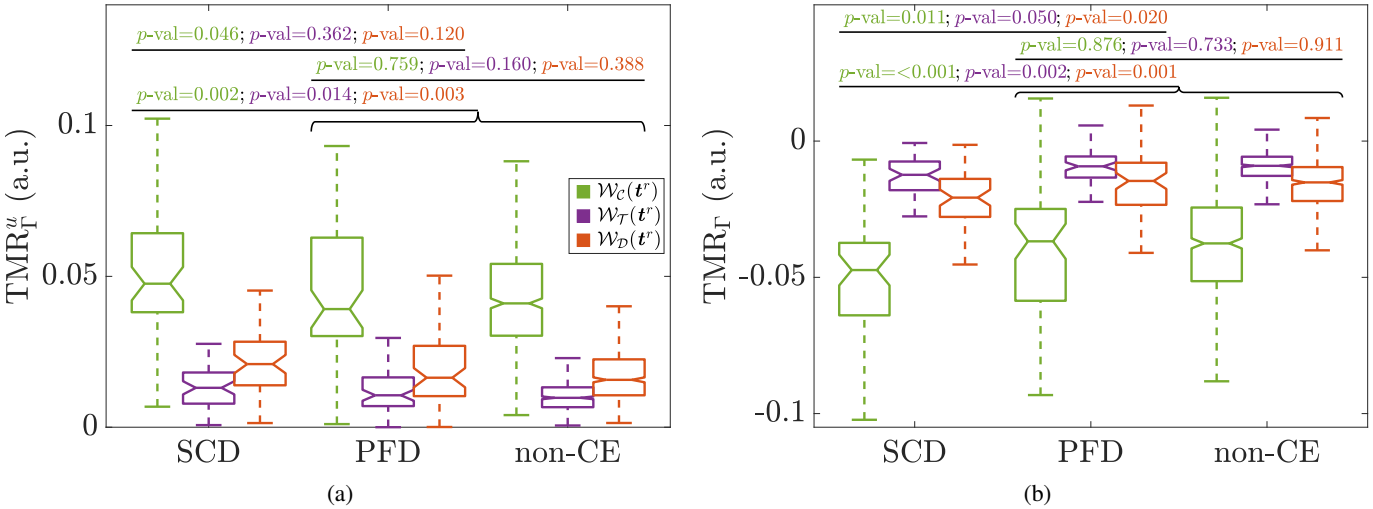

Fig. 7: Distributions of TMR^u_Γ and TMR_Γ (panels (a) and (b) respectively), for SCD, PFD and non-CE groups for $\Gamma \in \{\mathcal{C}, \mathcal{T}, \mathcal{D}\}$ (green, purple and orange, respectively). Mann-Whitney test p-values, colour coded for each WF, between SCD and PFD (uppermost row of p-val), PFD and non-CE (middle row of p-val) and SCD and the combination of PFD and non-CE groups (non-SCD) are highlighted with a curly bracket, (lower row of p-val).

As shown in Fig. 4, the $\mathcal{R}$ values (representing the relative error caused by those misplacements) were considerably lower for $d^u_{w,\mathcal{T}}$ and $d^u_{w,\mathcal{D}}$ with respect to $d^u_{w,\mathcal{C}}$ and similarly in case of $d_{w,\mathcal{T}}$ and $d_{w,\mathcal{D}}$ with respect to $d_{w,\mathcal{C}}$. This can be appreciate in the three tests (i.e. T_o only, T_e only and T_o-T_e symmetrically) by comparing the distributions of $\mathcal{R}_\mathcal{C}$ (in green) when no weighting was applied, with respect to $\mathcal{R}_\mathcal{T}$ (in purple) and $\mathcal{R}_\mathcal{D}$ (in orange) obtained after weighting with $\mathcal{W}_\mathcal{T}(\boldsymbol{t}^r)$ and $\mathcal{W}_\mathcal{D}(\boldsymbol{t}^r)$, respectively.

Moreover, across the three tests, smaller median and dispersion values were found for $\mathcal{R}_\mathcal{T}$ than for $\mathcal{R}_\mathcal{D}$, suggesting a slightly better performance of $\mathcal{W}_\mathcal{T}(\boldsymbol{t}^r)$ with respect to $\mathcal{W}_\mathcal{D}(\boldsymbol{t}^r)$ in terms of robustness against T_o and T_e mislabeling.

B. Simulated variability in an electrophysiological model

This test aimed to evaluate the impact of the proposed WFs on the physiological relevance of $d^u_{w,\Gamma}$ and $d_{w,\Gamma}$. The results obtained proved the preservation of the linear relationship between $d^u_{w,\Gamma}$ and $d_{w,\Gamma}$ and the changes in dispersion of repolarization at cellular level, which only varied by a proportional factor, as shown in Fig. 5 panels (b), (c) and (e), (f). These findings are in agreement with previous study [10] where only $d^u_{w,\mathcal{C}}$ was tested and found to linearly change with dispersion of repolarization as observed in this work.

A reduction in the sensitivity to changes in dispersion of repolarization can also be observed in $d^u_{w,\mathcal{T}}$ ($d_{w,\mathcal{T}}$) and $d^u_{w,\mathcal{D}}$ ($d_{w,\mathcal{D}}$) with respect to $d^u_{w,\mathcal{C}}$ ($d_{w,\mathcal{C}}$), in both scenarios 1 and 2. Moreover, values for $d^u_{w,\Gamma}$ and $d_{w,\Gamma}$ were found to be similar in absolute value but opposite in sign, since the increments

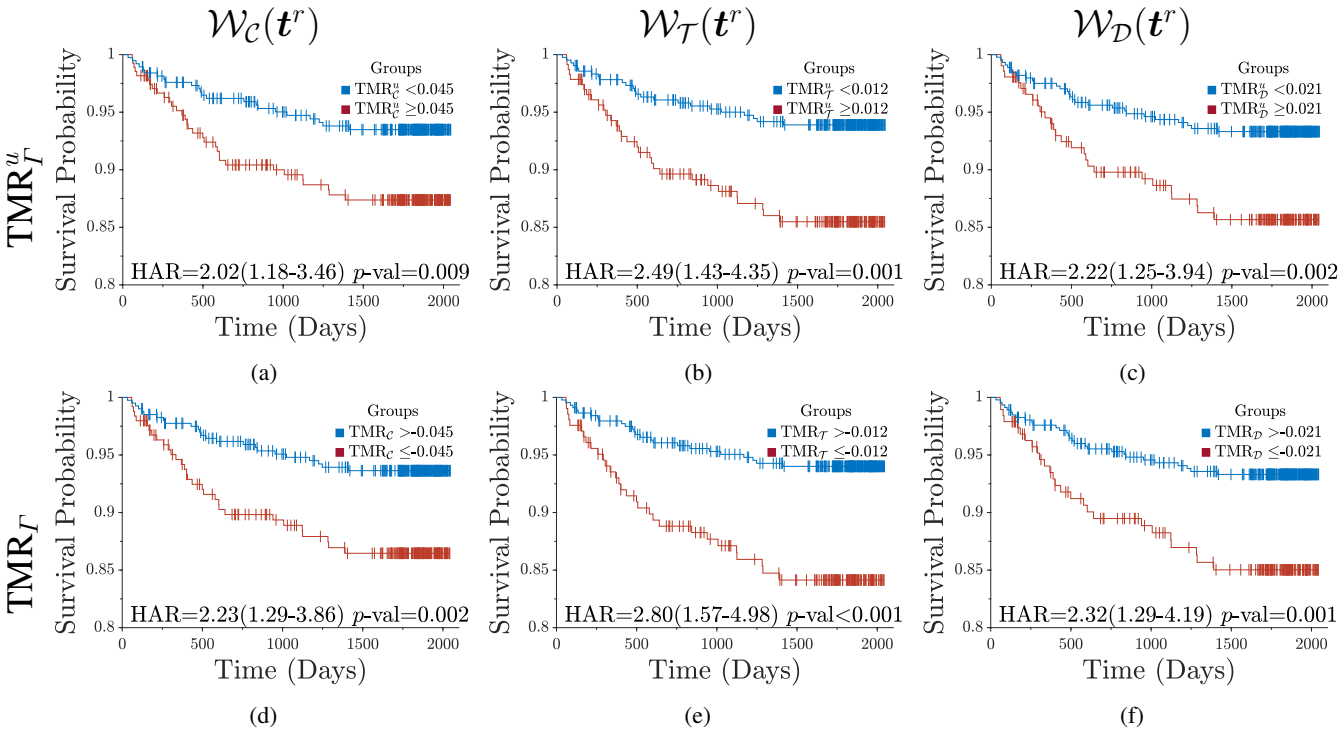

Fig. 8: Kaplan-Meier survival curves for the two groups defined after dichotomising patients in the MUSIC dataset according to the optimal threshold computed as described in section III-G. Curves for TMR^u_Γ and TMR_Γ (eq. (16)) are depicted in panels (a) to (c) and panels (d) to (f) respectively. In each panel, HAR value with corresponding 95% confidence intervals (CI) and p-val from the long-rank test are shown. Significant p-val were found for HAR in all the Cox analysis.

in σ led to TWs having larger magnitude and width than the reference one (black TW in Fig. 5a and Fig. 5d). Then, all simulated TWs had to be shrunk, i.e. negatively warped, to fit the reference.

C. Hemodyalisis dataset

A previous study [13] demonstrated that $d^u_{w,\mathcal{C}}$ and $d_{w,\mathcal{C}}$ were able to follow $\Delta[K^+]$ time-trend in patients undergoing HD. This capacity remained unaltered in this study regardless of the applied WF, being the differences in Pearson correlation negligible (Table II). However, the dynamic ranges of both $d^u_{w,\Gamma}$ and $d_{w,\Gamma}$ were reduced when a WFs was applied (Fig. 6), as also observed in the first simulation scenario in this study.

In other words, no particular improvement in monitoring [K^+] during the HD resulted from the addition of a weighting stage before time warping markers computation. This might be a consequence of the substantial TW morphological changes caused by $\Delta[K^+]$ in ESRD patients: TW narrowing and remarkable magnitude increment [26]–[29]. Then, TW morphology changes due to boundary location errors, which may or may not have occurred, seem to be negligible when compared to those driven by $\Delta[K^+]$, thus producing highly similar Pearson correlation values between markers and $\Delta[K^+]$.

D. MUSIC dataset

To evaluate the potential improvement of the TMR SCD risk stratification power when using the proposed WFs, CHF patients in sinus rhythm from the MUSIC study were analyzed.

Results from Mann-Whitney test (Fig. 7) demonstrated that both TMR^u_Γ and TMR_Γ are specific markers of SCD with no relation to PFD risk, regardless of the applied WF. Whereas the AUC (Table III) showed no clear advantages in using one of the proposed WF, we observed an improvement in accuracy (Table III) and in SCD risk prediction power of both $\text{TMR}^u_\mathcal{T}$ ($\text{TMR}_\mathcal{T}$) and $\text{TMR}^u_\mathcal{D}$ ($\text{TMR}_\mathcal{D}$) with respect to $\text{TMR}^u_\mathcal{C}$ ($\text{TMR}_\mathcal{C}$), thus demonstrating a better ability in distinguish between SCD and non-SCD, as visible from the Kaplan-Meier survival curves (Fig. 8).

We observed TMR_Γ provided the highest stratification power, Fig. 7b. This could be due to the avoidance of opposite-sign artifacts of similar absolute value, which may have been wrongly considered as regular values when using TMR^u_Γ (Fig. 7a). Moreover, the WF that led to the highest HAR values when using TMR_Γ was $\mathcal{W}_\mathcal{T}(\boldsymbol{t}^r)$, supporting its choice as WF when deriving TMR for future SCD risk stratification studies.

Lastly, it is worth to mention the similarity of $\text{TMR}^u_\mathcal{C}$ distribution for non-CE patients in the MUSIC study and those obtained from the UKBiobank recently published in [12].

E. Final considerations: Effects of weighting functions

The two studied WFs were designed to reduce the contribution of the boundary regions, and to explore different attenuation profiles. The main difference is that $\mathcal{W}_\mathcal{T}(\boldsymbol{t}^r)$ emphasises the peak region of the TW where the warping function typically gets close to zero values, an attenuating the extremes (Fig. 1d), while $\mathcal{W}_\mathcal{D}(\boldsymbol{t}^r)$ emphasises the slopes of the TW (Fig. 1c) resulting in a warping function, Fig. 1f, where

the central point of the two halves was emphasized, with the extremes also attenuated. This effect is particularly clear when comparing Fig. 1d, with respect to both Fig. 1e and Fig. 1f, and focusing on the extreme sections (light green area).

In the four studied scenarios, weighting with $\mathcal{W}_{\mathcal{T}}(\boldsymbol{t}^r)$ results in warping markers more robust to TW boundary location errors (see section V-A), leading to increased ability for SCD risk stratification than its counterpart $\mathcal{W}_{\mathcal{D}}(\boldsymbol{t}^r)$. This would indicate that useful physiological information may be overlooked when $\mathcal{W}_{\mathcal{D}}(\boldsymbol{t}^r)$ is applied. One possible explanation might be that the shape of this WF reduces, perhaps too sharply, the regions near the TW peak. Another reason might be that the regions around the TW boundaries are less attenuated than when using $\mathcal{W}_{\mathcal{T}}(\boldsymbol{t}^r)$, resulting in a reduced boundary misdetection attenuation effect.

Therefore, while $\mathcal{W}_{\mathcal{T}}(\boldsymbol{t}^r)$ is to be preferred to $\mathcal{W}_{\mathcal{D}}(\boldsymbol{t}^r)$ as WF in time warping analysis and subsequent TMR computation for SCD risk stratification, it seems that $\mathcal{W}_{\mathcal{D}}(\boldsymbol{t}^r)$ would result in $d^u_{w,\Gamma}$ and $d_{w,\Gamma}$ slightly better correlated with $\Delta[K^+]$. However, correlation coefficients are still very similar to draw strong conclusions about which is the most suitable WF for [K^+] monitoring.

F. Clinical significance

Findings from the present study prove the usefulness of the WFs in reducing the effects of TW location error when deriving biomarkers based on TW time warping analysis. Even though there were no significant changes in [K^+] monitoring in ESRD patients, a considerable improvement in SCD risk predicting values of the TMR index was observed, thus increasing its robustness and reliability for clinical applications.

G. Limitations and future works

Several limitations deserve to be mentioned. In this work, as in Ramírez *et al* [10], the van Oosterom equivalent double layer model was used to study the correlation between $d^u_{w,\Gamma}$ ($d_{w,\Gamma}$, respectively) and repolarization dispersion, but other biophysically detailed models of human ventricular electrophysiology [30], [31] could be used to further investigate the mechanisms underlying changes in repolarization dispersion reflected in variations in the analyzed warping-based indices.

The reduced number of patients in the HD dataset and available blood samples for each patient included in the study was a limitation to better frame the conclusion of the work. However, although there was no noticeable improvement in $\Delta[K^+]$ sensing by the application of the proposed WFs, they do not make results worse either, so applying WF by default in the signal processing pipeline would not decrease the usefulness of the d^u_w and d_w dispersion markers in the HD setting for monitoring [K^+].

Prospective studies are needed to corroborate the observations in [11], and reinforced here with the weighting marker versions, relative to the role of TMR in SCD risk prediction in CHF patients. Indeed this study considered consecutive patients, so the number of SCD victims was low, limiting the possibilities for further statistical analysis. The clinical validity and meaningfulness of the proposed WFs over extreme TW morphological variations, such as biphasic TWs, remains to be tested.

VI. Conclusion

T-wave morphology based markers derived from weighted time warping show improved robustness against the undesired effects of TW boundaries location errors without losing their physiological significance. In clinical settings, this improvement in robustness resulted in an enhancement of the SCD risk stratification value of the TMR index in CHF patients, but did not lead to a better ability to monitor [K^+] in HD patients.

Acknowledgment

This work was funded by Products & Technology S.L. (Castellbisbal, Barcelona, Spain), and by AGAUR, Generalitat de Catalunya (Spain) grant DI001-2018 and CIBER-BBN ref: "*DEKOALE*". The work was also supported by project PID2019-104881RB-I00, and PID2019-105674RB-I00 funded by Spanish Ministry of Science and Innovation (MICINN) and FEDER, by Gobierno de Aragón (Reference Group Biomedical Signal Interpretation and Computational Simulation (BSICoS)) T39-20R and projects LMP94-21, LMP141-21 cofunded by FEDER 2014-2020 "*Building Europe from Aragón*". J. Ramírez acknowledges the "María Zambrano" fellowship support from the European Union-NextGenerationEU and the support from the Marie Sklodowska-Curie grant No 786833. The computation was performed at the High Performance computing platform of the NANBIOSIS ICTS.

References

[1] P. Laguna, J. P. Martínez, and E. Pueyo, "Techniques for Ventricular Repolarization Instability Assessment from the ECG," *Proceedings of the IEEE*, vol. 104, no. 2, pp. 392–415, 2016.

[2] D. Panigrahy and P. K. Sahu, "P and T wave detection and delineation of ECG signal using differential evolution (DE) optimization strategy," *Australasian Physical & Engineering Sciences in Medicine*, vol. 41, pp. 225–241, 2018.

[3] R. Vecht, N. Peters, and M. A. Gatzoulis, "Basic principles," in *ECG Diagnosis in Clinical Practice*, pp. 1–9, London: Springer London, 2009.

[4] L. Sörnmo and P. Laguna, *Bioelectrical Signal Processing in Cardiac and Neurological Applications*. Academic Press, Elsevier Inc., 2005.

[5] M. S. Fuller, G. Sándor, B. Punske, B. Taccardi, R. S. MacLeod, P. R. Ershler, L. S. Green, and R. L. Lux, "Estimates of Repolarization Dispersion From Electrocardiographic Measurements," *Circulation*, vol. 102, no. 6, pp. 685–691, 2000.

[6] W. Zareba, F. Badilini, and A. J. Moss, "Automatic detection of spatial and dynamic heterogeneity of repolarization," *Journal of electrocardiology*, vol. 27 Suppl, no. SUPPL. 1, pp. 66–72, 1994.

[7] A. Mincholé, E. Pueyo, J. F. Rodríguez, E. Zacur, M. Doblaré, and P. Laguna, "Quantification of restitution dispersion from the dynamic changes of the T-wave peak to end, measured at the surface ECG," *IEEE Trans Biomed Eng*, vol. 58, no. 5, pp. 1172–1182, 2011.

[8] E. Pueyo, P. Smetana, P. Caminal, A. Bayes de Luna, M. Malik, and P. Laguna, "Characterization QT interval adaptation to RR interval changes and its use as a risk-stratifier of arrhytmic mortality in amiodarone-treated survivors of acute myocardial infarction," *IEEE Trans Biomed Eng*, vol. 51, pp. 1511–1520, 2004.

[9] S. M. Narayan, "T-wave alternans and the susceptibility to ventricular arrhythmias," *Journal of the American College of Cardiology*, vol. 47, no. 2, pp. 269–281, 2006.

[10] J. Ramírez, M. Orini, J. D. Tucker, E. Pueyo, and P. Laguna, "Variability of Ventricular Repolarization Dispersion Quantified by Time-Warping the Morphology of the T-Waves," *IEEE Trans Biomed Eng*, vol. 64, no. 7, pp. 1619–1630, 2017.

[11] J. Ramírez, M. Orini, A. Mincholé, V. Monasterio, I. Cygankiewicz, A. Bayés de Luna, J. P. Martínez, E. Pueyo, and P. Laguna, "T-Wave Morphology Restitution Predicts Sudden Cardiac Death in Patients With Chronic Heart Failure," *Journal of the American Heart Association*, vol. 6, no. 5, 2017.

[12] J. Ramírez, S. van Duijvenboden, N. Aung, P. Laguna, E. Pueyo, A. Tinker, P. D. Lambiase, M. Orini, and P. B. Munroe, "Cardiovascular Predictive Value and Genetic Basis of Ventricular Repolarization Dynamics," *Circulation*, vol. 12, no. 10, p. e007549, 2019.

[13] F. Palmieri, P. Gomis, D. Ferreira, J. E. Ruiz, B. Bergasa, A. Martín-Yebra, H. A. Bukhari, E. Pueyo, J. P. Martínez, J. Ramírez, and P. Laguna, "Monitoring blood potassium concentration in hemodialysis patients by quantifying T-wave morphology dynamics," *Scientific Reports*, vol. 11, no. 1, p. 3883, 2021.

[14] L. Xie, Z. Li, Y. Zhou, Y. He, and J. Zhu, "Computational Diagnostic Techniques for Electrocardiogram Signal Analysis," *Sensors*, vol. 20, no. 21, pp. 1–32, 2020.

[15] J. P. Madeiro, W. B. Nicolson, P. C. Cortez, J. A. Marques, C. R. Vázquez-Seisdedos, N. Elangovan, G. A. Ng, and F. S. Schlindwein, "New approach for T-wave peak detection and T-wave end location in 12-lead paced ECG signals based on a mathematical model," *Medical engineering & physics*, vol. 35, no. 8, pp. 1105–1115, 2013.

[16] R. Vazquez, A. Bayes-Genis, I. Cygankiewicz, D. Pascual-Figal, L. Grigorian-Shamagian, R. Pavon, J. R. Gonzalez-Juanatey, J. M. Cubero, L. Pastor, J. Ordonez-Llanos, J. Cinca, and A. B. de Luna, "The MUSIC Risk score: a simple method for predicting mortality in ambulatory patients with chronic heart failure," *European heart journal*, vol. 30, no. 9, pp. 1088–1096, 2009.

[17] J. P. Martínez, R. Almeida, S. Olmos, A. P. Rocha, and P. Laguna, "A wavelet-based ECG delineator: evaluation on standard databases," *IEEE Trans Biomed Eng*, vol. 51, pp. 570–581, 2004.

[18] J. García, M. Aström, J. Mendive, P. Laguna, and L. Sörnmo, "ECG-based detection of body position changes in ischemia monitoring," *IEEE Trans Biomed Eng*, vol. 50, no. 6, pp. 677–685, 2003.

[19] "Recommendations for measurement standards in quantitative electrocardiography," *European Heart Journal*, vol. 6, no. 10, p. 815–25, 1985.

[20] A. Van Oosterom, "Genesis of the T wave as based on an equivalent surface source model," *Journal of Electrocardiology*, vol. 34, no. 4, pp. 217–227, 2001.

[21] N. J. Perkins and E. F. Schisterman, "The Inconsistency of "Optimal" Cut-points Using Two ROC Based Criteria.," *American journal of epidemiology*, vol. 163, no. 7, p. 670, 2006.

[22] J. M. Bland and D. G. Altman, "Statistics Notes: Survival probabilities (the Kaplan-Meier method)," *BMJ : British Medical Journal*, vol. 317, no. 7172, p. 1572, 1998.

[23] J. T. Rich, J. G. Neely, R. C. Paniello, C. C. J. Voelker, B. Nussenbaum, and E. W. Wang, "A practical guide to understanding Kaplan-Meier curves," *Otolaryngology–head and neck surgery : official journal of American Academy of Otolaryngology-Head and Neck Surgery*, vol. 143, no. 3, p. 331, 2010.

[24] E. Marubini and M. G. Valsecchi, *Analysing survival data from clinical trials and observational studies*. Chichester (UK): J. Wiley and Sons, 2004.

[25] D. Y. Lin, L. Dai, G. Cheng, and M. O. Sailer, "On Confidence Intervals for the Hazard Ratio in Randomized Clinical Trials," *Biometrics*, vol. 72, no. 4, p. 1098, 2016.

[26] A. Lanari, L. O. Chait, and C. Capurro, "Electrocardiographic effects of potassium. I. Perfusion throught the coronary bed.," *Am Heart journal*, vol. 67, no. 3, pp. 357–363, 1964.

[27] M. M. Laks and S. R. Elek, "The effect of potassium on the electrocardiogram: clinical and transmembrane correlations," *Diseases of the chest*, vol. 51, no. 6, pp. 573–586, 1967.

[28] N. El-Sherif and G. Turitto, "Electrolyte disorders and arrhythmogenesis," *Cardiol J.*, vol. 3, no. 18, pp. 233–45, 2011.

[29] J. T. Levis, "ECG diagnosis: hyperkalemia.," *The Permanente journal*, vol. 17, no. 1, p. 69, 2013.

[30] R. H. Clayton, O. Bernus, E. M. Cherry, H. Dierckx, F. H. Fenton, L. Mirabella, A. V. Panfilov, F. B. Sachse, G. Seemann, and H. Zhang, "Models of cardiac tissue electrophysiology: Progress, challenges and open questions," *Progress in Biophysics and Molecular Biology*, vol. 104, no. 1-3, pp. 22–48, 2011.

[31] S. A. Niederer, J. Lumens, and N. A. Trayanova, "Computational models in cardiology," *Nature Reviews Cardiology*, vol. 16, no. 2, pp. 100 – 111, 2019.